

Temperature-Dependent Infrared Spectroscopy Studies of a Novel Antiferroelectric Liquid-Crystalline Thiobenzoate

Kacper Druzbicki,^{*,†,‡} Antoni Kocot,^{§,||} Edward Mikuli,[†] Mirosława Danuta Ossowska-Chruściel,[⊥] and Janusz Chruściel[⊥]

[†]Department of Chemical Physics, Faculty of Chemistry, Jagiellonian University, Ingardena 3, 30-060, Cracow, Poland

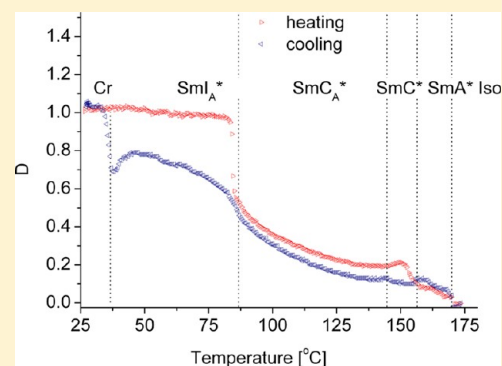
[‡]Frank Laboratory of Neutron Physics, Joint Institute for Nuclear Research, 141980 Dubna, Russia

[§]Department of Biophysics and Molecular Physics, Institute of Physics, University of Silesia, Uniwersytecka 4, 40-007 Katowice, Poland

^{||}Department of Electronic and Electrical Engineering, Trinity College Dublin, Dublin 2, Ireland

[⊥]Department of Technology and Chemical Physics, Institute of Chemistry, University of Natural Sciences and Humanities, 3-go Maja 54, 08-110 Siedlce, Poland

ABSTRACT: The temperature-dependent infrared spectroscopy studies of one novel antiferroelectric liquid crystal (AFLC), known under the MHPSBO10 acronym, have been undertaken. The FT-IR measurements have been performed for homeotropic and planar heterogeneous sample geometries. The main order parameters have been determined and followed with temperature. The presented study delivers complex insight into the evolution of the vibrational spectrum upon phase transitions, covering the whole mesophase range. The experimental studies have been supported by theoretical studies of MHPSBO10 in confined geometries.



INTRODUCTION

It has been shown that the vibrational spectroscopy of liquid crystals could be an extremely powerful tool in a great number of phase transition studies that can be investigated by both IR and Raman techniques. The use of IR spectroscopy for the study of liquid crystals was initiated in the mid 1960s,¹ when the simple expression for the IR dichroism in terms of *S* order parameter had already been worked out by Maier and Saupe.² Since the 1970s, however, the technique has been rather sparingly used in the literature. Most efforts were made to understand the recorded spectral data since most of the mesogens exhibit an extremely complex vibrational dynamics due to a large molecular size described by a low symmetry.^{3–5} In the 1980s Fontana et al. also proved the vibrational spectroscopy to be a valuable tool in the molecular dynamics studies of some simpler nematic systems.^{6,7} The molecular reorientation studies in the far-infrared range were also reported by Janik's team.^{8,9} However, the rebirth of vibrational spectroscopy in the discussed field was observed in the 1990s, mainly along with the progression of the ferroelectric smectics studies. Since the early works by Kocot et al. dealing with order parameters and molecular tilt angle,^{10–14} many papers presenting successful application of infrared spectroscopy were reported.^{15–18} In parallel, significant papers by Kim et al.^{19–21} have confirmed the applicability of Raman spectroscopy in related studies and opened the discussion for antiferroelectric

liquid crystals. Most experiments have been performed for planar sample configuration; however, in the early 2000s, the alternative way of studying the most important order parameters and the molecular tilt angle was proposed.^{22,23} Finally, vibrational spectroscopy has become a relevant tool in the studies of de Vries type²⁴ or biaxial nematic phases.^{25–27} As modern quantum chemistry allows us to predict the vibrational spectra with very good accuracy, the experimental data may be nowadays deeply understood and interpreted, giving even further information about the components of the related transition moments, despite the high complexity of the recorded data.^{28–31}

Recently, the vibrational spectrum of MHPSBO10 has been extensively analyzed in terms of solid-state oriented quantum-chemical calculations and presented elsewhere,³² delivering unambiguous knowledge of band assignment, their composition, and the related transition moment geometry. Such knowledge in relation with the spectra observed for the samples in confined geometries allows us to probe directly the structural properties of mesophases at the molecular level, building a bridge between the macroscopic and molecular

Received: May 25, 2012

Revised: August 15, 2012

Published: August 21, 2012

sample properties, which may be quantifiably defined in terms of the order parameters.

Hence, the main goal of this paper is to present the temperature-dependent middle range infrared measurements, performed for homeotropic and planar heterogeneous sample geometries, giving insight into the evolution of the vibrational spectrum within all the mesophases. The structural changes are quantitatively described in the frame of presented order parameters and followed with temperature. The experimental work is supplemented by the theoretical infrared spectra calculated for MHPSBO10 in confined geometries.

Characteristics of MHPSBO10. The chemical structure of MHPSBO10 is presented in Figure 1a.

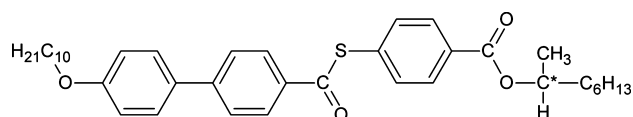


Figure 1. (S)-1-Methylheptyl-4-(4'-decyloxybiphenylthiocarboxy)-benzoate (MHPSBO10).

The compound under study is the highest homologue from the (S)-MHPSBO_n series, which is analogous to the family of the first known antiferroelectric compound MHPOBC, differing in the replacement of the ester group by a softer thioester bridge.³³ The compound exhibits rich polymorphism, including both ferro- (SmC*) and antiferroelectric (SmC_A*, SmI_A*) as well as paraelectric (SmA*) smectic phases, which makes the compound an interesting object of complex physicochemical studies. The complementary studies of the mesomorphic properties have been performed by the use of many complementary techniques, namely, Differential Scanning Calorimetry (DSC), Polarization Microscopy (POM), Transmitted Light Intensity (TLI), Electrooptical Methods, as well as Dielectric Spectroscopy, and have been recently presented in ref 34. As the highest homologous compound in the series, the phase transitions for MHPSBO10 may be observed at the lowest temperature values. No ferroelectric subphases were detected for the title compound. Table 1 presents the polymorphism of MHPSBO10 along with the corresponding temperatures determined using DSC with the heating/cooling rate of 2 °C/min and with FT-IR spectroscopy in both homeotropic and planar cell configurations, as described further on. As may be seen in the table, the phase transitions within the mesophases are accompanied by small thermodynamic effects, which correspond to very subtle spectral differences which are hardly observed for the unaligned sample with the isotropic dipole distribution. One may also observe a high metastability of the SmI_A* phase, which strongly depends on the experimental cooling dynamics. Upon heating, this phase is observed in a very narrow temperature range. The compound reveals strong temperature dependence on many macroscopic properties like spontaneous polarization, rotational viscosity, or molecular tilt angle. The main goal of this paper is to probe the temperature dependence of the MHPSBO10 infrared spectrum and to determine the main order parameters, allowing us to link the macroscopic sample properties with the molecular level.

Experimental and Computational Details. The compound was synthesized and optically purified by Ossowska-Chrusciel as presented in the original paper.³³ The vibrational spectra were recorded for the samples oriented in both homeotropic and planar cell configurations. In the latter case

Table 1. Phase Polymorphism in MHPSBO10 as Studied with DSC and FT-IR Measurements in Homeotropic (HT) and Planar (PL) Cell Configuration

Cooling					
Iso → SmA* → SmC* → SmC _A * → SmI _A * → Cr					
phase transition	ΔH	ΔS	DSC	FT-IR (HT)	FT-IR (PL)
	kJ/mol	J/mol·K	observed transition [°C]		
Iso → SmA*	5.05	11.52	165.4	170.0	170.0
SmA* → SmC*	0.59	1.38	153.2	156.5	157.0
SmC* → SmC _A *	0.07	0.17	142.9	144.5	143.0
SmC _A * → SmI _A *	0.61	1.70	85.6	87.0	86.0
SmI _A * → Cr	14.48	49.48	19.6	36.5	55.0
Heating					
Cr → SmI _A * → SmC _A * → SmC* → SmA* → Iso					
phase transition	ΔH	ΔS	DSC	FT-IR (HT)	FT-IR (PL)
	kJ/mol	J/mol·K	observed transition [°C]		
Cr → SmI _A *	30.24	84.93	83.1	84.5	-
SmI _A * → SmC _A *	0.52	1.43	86.3	86.0	-
SmC _A * → SmC*	0.07	0.17	144.3	146.5	-
SmC* → SmA*	0.35	0.81	153.8	156.5	-
SmA* → Iso	5.39	12.27	166.2	170.0	-

an IR-KRS5 grid polarizer was used to polarize the IR beam. The studied samples were sandwiched between two ZnSe windows which were spin-coated with orienting layers. Carboxylatochromium complexes (Chromolane) solution (2%) in isopropanol, baked at 150 °C, was used to induce the homeotropic alignment, while the planar orientation was induced by polyamic acid RN-1175 (Nissan Chemical Industries) polymerized at 225 °C and rubbed in one direction. Mylar films (~2 μm thick) have been used as spacers, which resulted in 5.2 and 5.4 μm thick cells in the former and latter configurations, respectively. The cell thickness was determined from the interference patterns measured before introducing the sample. The texture observation under the polarized light confirmed the perfect homeotropic alignment in the former case. However, despite many attempts, including the use of different orienting layers, we were unable to obtain the homogeneously aligned planar sample. For the planar configuration, the ZnSe substrates were additionally coated with indium tin oxide (ITO). However, the field-induced ordering was ineffective for thicker samples, while for the thinner ones it resulted with electrical circuits, probably due to the inhomogeneity of the ITO cover surface. Hence, we prepared possibly the thinnest sample cell, to suppress the helix formation and minimize the multidomain texture. The cells were capillary filled a few degrees above the transition to the isotropic phase. All experiments were carried out using a Bio-Rad FTS-6000 Fourier transform infrared spectrometer equipped with DTGS detector, KBr beamsplitters, and Globar infrared source. The spectra were collected in the 4000–550 cm⁻¹ frequency range, with accumulation over 16 scans and the spectral resolution of 2 cm⁻¹. The temperature was stabilized for 300 s for each point using a homemade controller with <0.05 °C accuracy. The spectra were recorded every 0.5 and 1 °C for the homeotropic and planar samples, respectively. The previous studies revealed a well-defined phase situation with no significant differences between the cooling and heating cycles, despite the high metastable SmI_A* phase which was observable

upon heating only in a very narrow temperature range. Hence, to confirm the spectral reproducibility, the studies in homeotropic orientation were also performed upon heating for the sample left overnight in the crystalline phase. To avoid the overheating effects, we mainly focus on the cooling cycle. The infrared bands chosen for further consideration were analyzed directly when possible, while the overlapped ones were deconvoluted with a numerical approximation of the Voigt function. For the strongly overlapped bands near $\sim 3000 \text{ cm}^{-1}$, the Lorentzian functions were used in order not to overload the number of the fitting parameters. The numerical deconvolution was performed with PeakFit ver. 4.1 (from Systat Inc., USA). Along with the vibrational spectroscopy experiments, the high quality calculations of molecular structures and their vibrational spectra were performed with Density Functional Theory (DFT). The extensive vibrational analysis has been recently presented with details in ref 32 and will not be described here again. In the present work we extend the reported vibrational analysis by exploring the theoretical polarized and homeotropic infrared spectra, giving further insight into the transition dipole moment compositions and their distribution along the normal modes. In addition to the previously reported results,³⁴ we have supplemented our studies by performing the birefringence measurements. The interferometric measurements were performed upon cooling for a thick $54.7 \mu\text{m}$ cell using an Ocean Optics USB 2000 fiber coupled UV–vis optical spectrometer, equipped with halogen lamp.

Infrared Absorbance Components in the Experimental Conditions. At a molecular level, the infrared absorption depends on the angle between the molecular transition dipole moment associated with the particular normal mode and the direction of the electrical vector of the incident light. For the isotropic system, the distribution of the transition dipole moments is direction independent, hence it is equally averaged all over the space. However, in the orientationally ordered systems, the absorbance components become dependent on the angle between the alignment axis and the polarization direction of the incident light. Since for any anisotropic system the absorbance is the second-rank tensor property, it may be expressed in terms of transition dipole moments and order parameters. The exact expressions were described in detail, e.g., in refs 22 and 25.

In the laboratory frame, the main tensor components may be expressed as the following

$$\begin{aligned}
 A_X/A_0 &= 1 + (S - P)\left(\frac{3}{2}\sin^2\beta - 1\right) \\
 &\quad + \frac{1}{2}(D - C)(\sin^2\beta \cos 2\varphi) \\
 A_Y/A_0 &= 1 + (S + P)\left(\frac{3}{2}\sin^2\beta - 1\right) \\
 &\quad + \frac{1}{2}(D + C)(\sin^2\beta \cos 2\varphi) \\
 A_Z/A_0 &= 1 + S(2 - 3\sin^2\beta) - D\sin^2\beta \cos 2\varphi \quad (1)
 \end{aligned}$$

where A_0 is an average absorbance $(A_X + A_Y + A_Z)/3$, while β and φ are the Euler's angles of the transition dipole moment. S , D , P , and C are the second rank order parameters representing the three diagonal Saupe ordering matrices, one for each of the three axes $i = X, Y, Z$, described as

$$\begin{aligned}
 S &\equiv S_{zz}^Z; \quad D \equiv S_{xx}^Z - S_{yy}^Z; \quad P \equiv S_{xx}^X - S_{zz}^Y; \\
 C &\equiv (S_{xx}^X - S_{yy}^X) - (S_{xx}^Y - S_{yy}^Y) \quad (2)
 \end{aligned}$$

where $S_{\alpha\beta}^i = \langle 1/2(3l_{i\alpha}l_{i\beta} - \delta_{\alpha\beta}) \rangle$, $\alpha = x, y, z$, and $l_{i\alpha}$ is the cosine of the angle between the molecular axis α and laboratory axis i .

For a uniaxial molecule, the long axis ordering is described by S , while the phase biaxiality is described by P , expressing an average tilting of molecules. For biaxial molecules, the order parameter D describes the short axes ordering and biasing of the rotation over the molecular long axis. If the studied phase is uniaxial and the effect of molecular interaction and the local field can be ignored, the absorbance may be expressed only in terms of parallel and perpendicular components with respect to the optical axis, which depends only on two main order parameters, namely, S and D . Finally, in the biaxial phases built by biaxial molecules, the coupling between P and D needs to be described by introducing the C order parameter.

The experimental conditions have been presented in Figure 2. In the homeotropic alignment, the nonpolarized IR beam is

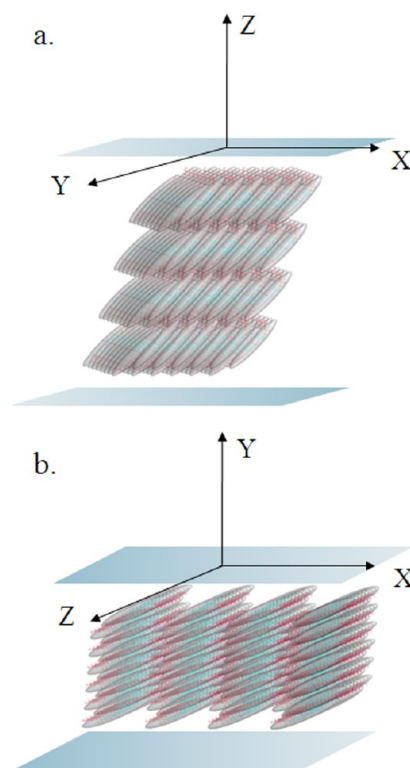


Figure 2. Idealized picture of the MHPBSO10 tilted phase in homeotropic (a) and planar (b) configuration within the chosen laboratory frame.

parallel to the smectic layer normal, along with the laboratory Z axis (as may be seen in Figure 2a), and there are all possible orientations of the tilting direction around the smectic layer normal. Hence, the experiments using the homeotropic cell are independent of the presence of the helical structure. The A_Z component is not measured in such configurations, thus the observed absorbance may be described as

$$A_{\text{HT}} = (A_X + A_Y)/2A_0$$

$$= 1 + S\left(\frac{3}{2} \sin^2 \beta - 1\right) + \frac{1}{2}D(\sin^2 \beta \cos 2\varphi) \quad (3)$$

The given expression allows us to determine the S and D order parameters, by the usage of separate bands corresponding to transition dipole moments of opposing geometry.

The complete set of four order parameters may be obtained only for the combination of two experiments, performed in both homeotropic and planar alignments. As may be seen in Figure 2b, the laboratory frame is rotated here by 90° , and the A_Z and A_X components may be directly obtained. The third component may be derived based on the homeotropic measurements

$$A_Y = 2A_{\text{HT}} - A_Z \sin^2 \theta - A_X \cos^2 \theta \quad (4)$$

where θ stands for the molecular tilt angle.

If the components in the direction of the three axes are known along with the transition dipole geometries for the selected opposing bands, then the complete set of order parameters may be determined by solving the set of eqs 2.

In practice, the problems with homogenization of antiferroelectric liquid crystals limits the related physicochemical studies. However, the big advantage of homeotropic cell measurements is their independence of the helical structure presence, allowing us to obtain the more reliable values of—probably the most important— S and D parameters. We stumbled on such problems across our work, hence we mainly focused on the homeotropic cell configuration.

General Discussion of the Infrared Spectra. The full interpretation of the MHPBSO10 vibrational spectrum was based on the FT-IR and FT-RS measurements supported by extensive modern quantum-chemical calculations. As mentioned before, such data along with the discussion of the vibrational transition moments were presented in detail elsewhere.³² On the basis of the previously reported computations, we take further insight into the absorbance components by studying the system in confined geometries. Here, instead of the reported QUANTUM ESPRESSO (QE) results, we present the same quality CASTEP³⁵ data obtained with exactly the same computational conditions to get the further absorbance components which were not delivered by the QE computations.

Figure 3a delivers the experimental FT-IR spectra compared with the theoretical ones obtained by taking the perpendicular absorbance components using several theoretical models as described in ref 32. The selected homeotropic spectra, recorded in the SmA* and crystal phases, are compared with the isotropic one. In the Figure 3b the corresponding polarized spectra are presented as their perpendicular (\perp) and parallel (\parallel) components. The theoretical calculations predicted the anisotropic infrared spectra with a very good overall accuracy, confirming a proper decomposition of the transition dipole moments. The insight into the computed anisotropic infrared spectra shows that most of the prominent spectral features are of parallel polarization. The theoretical calculations clearly predict the absorbance anisotropy of a particular band which is directly related with the geometry of the transition of the dipole moment. Hence the sharpest anisotropy is connected with the orientations directed along the molecular long axis. The most prominent parallel bands may be observed at ~ 1600 ($\nu\text{C}=\text{C}$ in phenyl ring); around ~ 1500 (assigned to the coupled

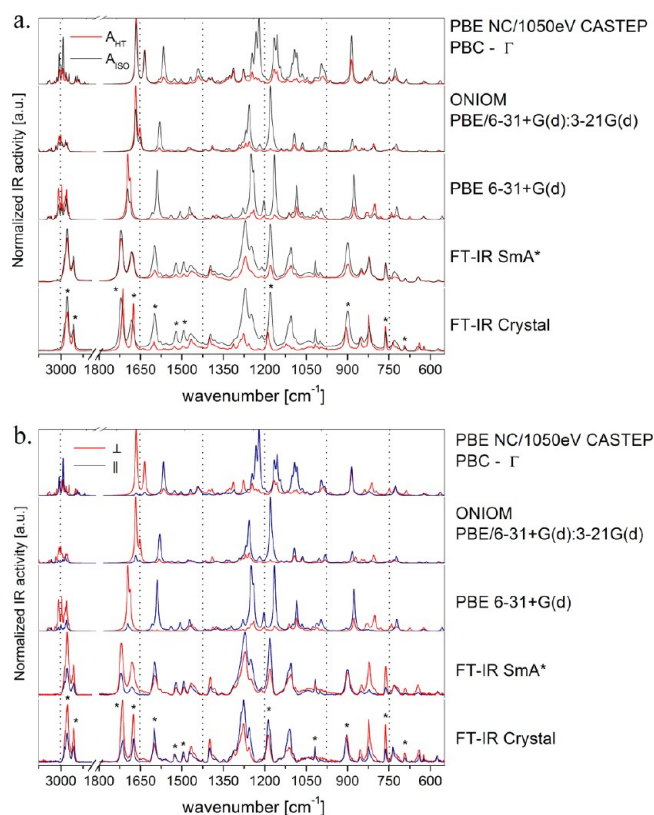


Figure 3. Experimental FT-IR spectra of MHPBSO10 compared with the unscaled theoretical ones. The homeotropic spectra (a) presented along with the isotropic ones. The polarized spectra (b) presented as their perpendicular (\perp) and parallel (\parallel) components. The most prominent bands were denoted with asterisks.

antisymmetric stretching and deformation modes of the biphenyl part) or ~ 1300 (assigned to the set of deformations within the alkyl chains); at ~ 1200 (in-plane C–H deformations within the biphenyl part); or as the set of overlapped bands near $\sim 1100 \text{ cm}^{-1}$ (mainly linked with the stretchings within the alkyl parts). The most significant perpendicular bands are the ones near 1715 cm^{-1} , assigned to the isolated $\nu\text{C}=\text{O}$ stretchings, as well as the isolated band at $\sim 760 \text{ cm}^{-1}$ corresponding to the C–H out-of-plane deformation of the ring linked with the chiral part or the out-of-plane deformations of the biphenyl group near 900 cm^{-1} .

Since such a complex vibrational spectrum consists of many overlapping bands, mostly related to significantly coupled normal modes, not all the vibrations may be further experimentally studied in detail. The most significant bands, taken for the analysis and discussed further on, are denoted in Figure 3 with asterisks (*). The selected bands are: of relatively strong intensity in the whole temperature range, well separated, and related with the isolated or well-defined vibrations by the transition dipole moment.

Transition Dipole Moments. Figure 4 collects the rotation angle dependence of the integral intensities for the selected bands, as observed in SmA* and crystal phases of the planar aligned MHPBSO10 sample. The ω angle between the layer normal and the polarization of an incident radiation is taken as zero when these two directions coincide with each other. The profiles were fitted using the following relation

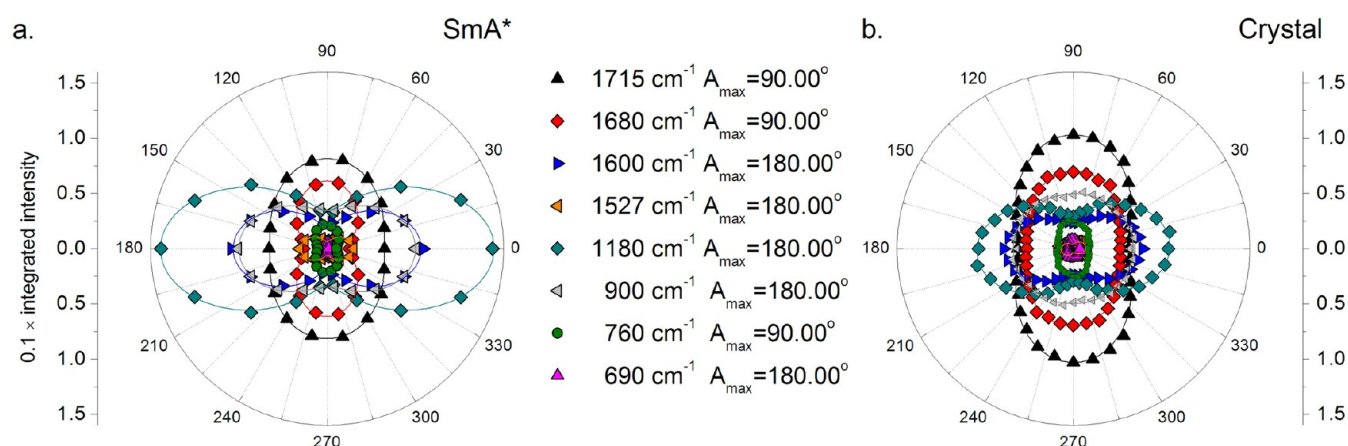


Figure 4. Circular graphs of the absorbance vs the polarizer rotation angle ω for the most prominent bands in the SmA* and crystal phases of MHPSBO10 as observed for the planary aligned sample upon cooling.

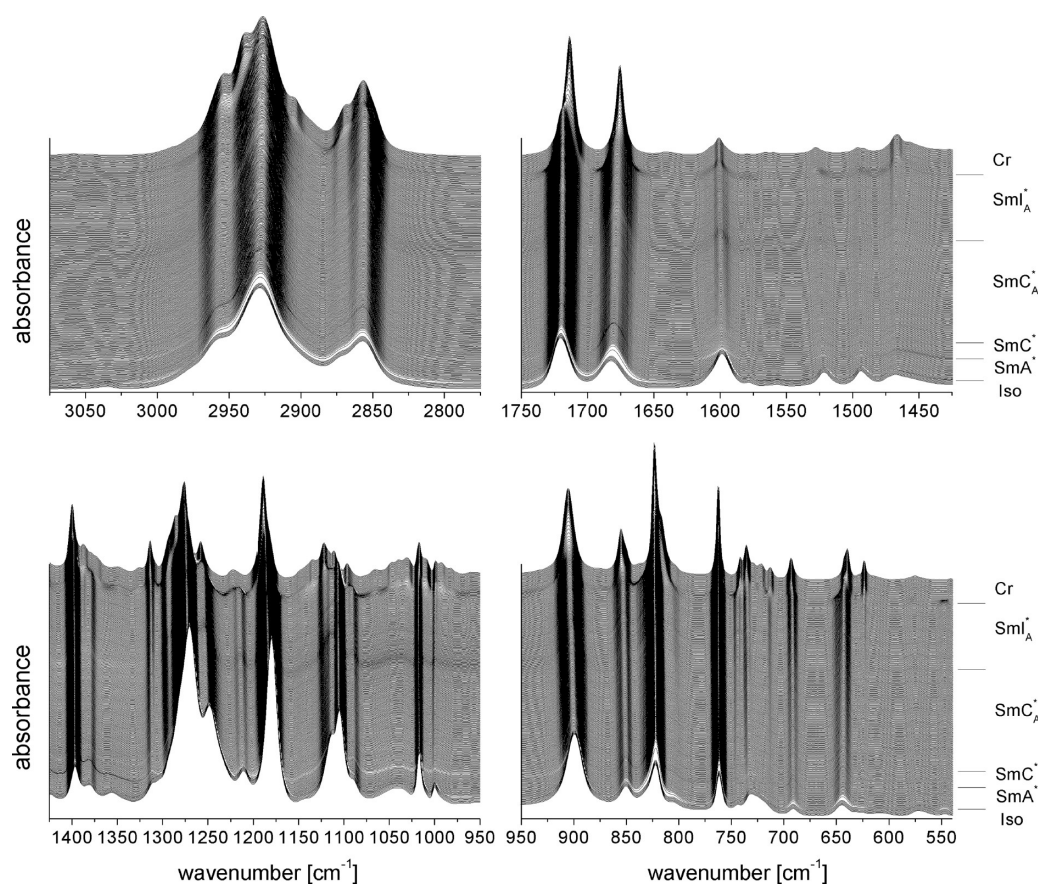


Figure 5. Middle FT-IR spectra of the homeotropic MHPSBO10 sample recorded upon cooling presented every 0.5 °C from the isotropic (173.5 °C) down to the crystal phase (27.1 °C). For transparency, the spectra were divided into separate ranges.

$$A(\omega) = -\log[10^{-A_{\max}} + (10^{-A_{\min}} - 10^{-A_{\max}})\sin^2(\omega - \omega_0)] \quad (5)$$

where A_{\max} and A_{\min} are the maximal and minimal values of the absorbance; ω is the polarizer angle; and ω_0 is the angle for which the maximal absorbance is obtained.

Assuming that there is no local biaxial order, and hence molecules are freely rotating along their long axes (SmA* phase), the observed dichroic ratio R was expressed in relation with the molecular tilt as the following³⁶

$$R = \frac{A_{\max}}{A_{\min}} = \frac{\frac{1}{2} \sin^2 \beta (1 - \langle \cos^2 \theta \rangle) + \cos^2 \beta \langle \cos^2 \theta \rangle}{\frac{1}{4} \sin^2 \beta (1 + \langle \cos^2 \theta \rangle) + \frac{1}{2} \cos^2 \beta (1 - \cos^2 \theta)} \quad (6)$$

where the β angle describes the deviation of the transition dipole moment from the molecular long axis and θ stands for the molecular tilt angle. By knowing the molecular tilt, such an expression may be used to determine the β angle for a perpendicular transition dipole moment. For the transition

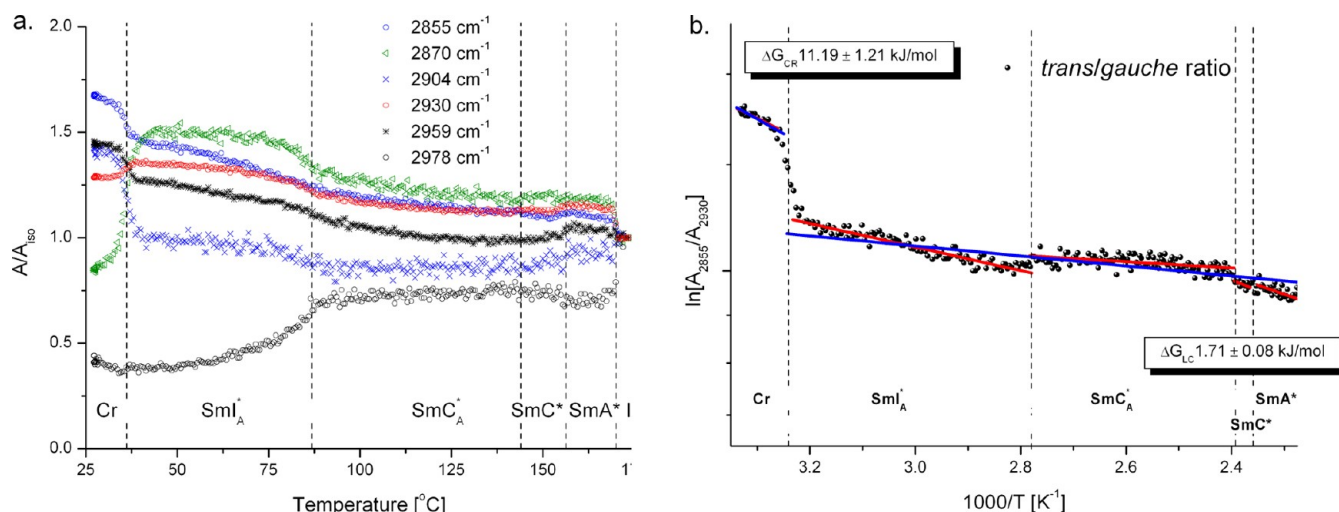


Figure 6. Temperature evolution of the normalized integral intensities in the $\nu\text{C-H}$ stretching region (a) recorded for the homeotropic MHPSBO10 sample. The bands near 2855 and 2930 cm^{-1} were assigned to the symmetric and asymmetric CH_2 stretchings, respectively, for which the intensity ratios were used to probe the thermal evolution of the *trans/gauche* conformer distributions (b).

moments parallel to the molecular long axes, the relation 6 was multiplied by the orientational order parameter defined as the following

$$S = \frac{A_{\max} - A_{\min}}{A_{\max} + 2A_{\min}} \quad (7)$$

The experimental β angles for particular transitions were determined assuming the molecular tilt of 26° (see further text for the explanation) and $S = 0.54$ determined for the planar aligned sample. Table 1 collects the frequencies of the most prominent FT-IR bands with their approximate assignment, along with Euler's angles associated with particular modes as observed experimentally and predicted by DFT computations.

The β angle computed with the molecular modeling approach was defined as an angle between the transition dipole moment and the lowest component of the moment of inertia tensor. The φ angle defines the orientation of the transition dipole moment in the XY plane. In the case of Periodic Boundary Calculations (PBCs), the symmetric transition moment tensor was defined within the unit cell frame, built by two antiparallel mesogens. It depends on the absolute orientation of the simulation cell in the Cartesian space. Hence, the β angle was defined here with respect to the c lattice constant (in the direction of the molecular long axis).

The theoretical predictions stay in very good agreement with the experimental values, giving an overall agreement close to $\sim 5^\circ$ but differing noticeably between the particular modeling approaches. However, the possible influence of intermolecular interactions on the transition moment geometry is rather lower than $<10^\circ$, as may be deduced from the comparison of the PBE and ONIOM data (the isolated molecule and cluster approaches at the PBE/6 + 31G(d) level). The computations confirmed the general differences between the particular transition moments as observed experimentally.

Temperature-Dependent Infrared Spectra. Figure 5 collects the temperature-dependent FT-IR spectra recorded for the homeotropic MHPSBO10 sample upon cooling, starting from the isotropic down to the crystal phase. As one may see, the temperature evolution reveals very subtle continuous changes in all the presented frequency regions, which are

hardly observed for the unaligned sample, as was indicated by our background measurements.

Alkyl Chains. Since the studied mesogen consists of unsubstituted alkyl chains in both terminal parts, the spectral range $\sim 3000\text{ cm}^{-1}$ delivers average information about the alkyl chains ordering, which cannot be further resolved into the separate chain contributions. The quoted range was deconvoluted using the Lorentzian functions, and the normalized absorbance for particular bands was presented in Figure 6a. The bands observed at ~ 2855 and 2870 cm^{-1} may be assigned to the symmetric stretching modes of the methylene $\nu_{\text{ss}}\text{CH}_2$ and methyl $\nu_{\text{ss}}\text{CH}_3$ groups, respectively. The bands found at ~ 2900 and 2930 cm^{-1} were assigned to the antisymmetric stretchings of the methylenes $\nu_{\text{ass}}\text{CH}_2$. Finally, the bands over $\sim 2950\text{ cm}^{-1}$ were assigned to the in-plane and out-of-plane methyl νCH_3 stretchings. The analysis of the high frequency region was reported to be a valuable tool in the determining of the *trans/gauche* conformers' population ratios.^{37–39} Such a phenomenon may be studied by probing the intensity relations for the 2855 and 2930 cm^{-1} bands which may be linked with the particular conformer populations.

From statistical thermodynamics, the *trans/gauche* relation is governed by the free energy difference, ΔG , between the two conformational isomers, as expressed by the following equation³⁹

$$\frac{n_{\text{trans}}}{n_{\text{gauche}}} \propto \exp \frac{-\Delta G}{RT} \quad (8)$$

where n_{trans} and n_{gauche} are the number of units in the *trans* and *gauche* conformations, respectively. It should be noted that n_{gauche} is the summation of the two *gauche* forms, and ΔG is the free energy difference.

Although the spatial distribution of the transition dipole moments associated with the alkyl chains comes also from molecule tilting and phase ordering, affecting the observed absorbance, an approximate ratio may be directly probed upon temperature within the ordered crystal and the liquid crystal phases, as presented in Figure 6b. The free energy difference in the solid state was estimated as $\Delta G = 11.2\text{ kJ/mol}$, while an average value in the mesophases equals 1.71 kJ/mol . By analyzing the temperature dependence of the determined ratio,

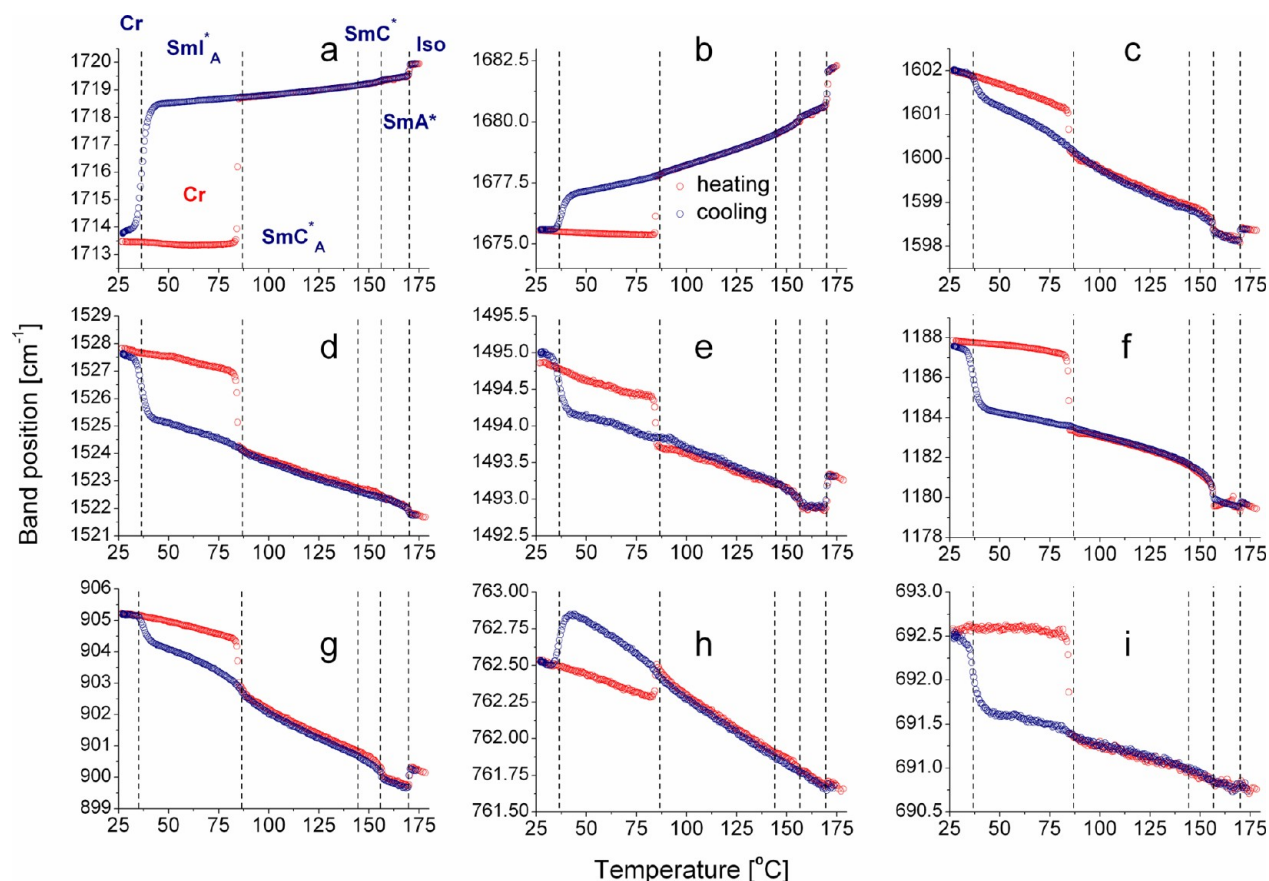


Figure 7. Temperature evolution of the wavenumbers for the most prominent bands of the MHPSBO10 sample in homeotropic orientation as observed by temperature-dependent infrared spectroscopy. Cooling and heating cycles colored in blue and red, respectively. The bands were labeled with the lowercase letters as defined in Table 2.

we may notice an increase of the disorder within alkyl chains through the SmC^* and SmA^* phases, which may be related with an increase of the short axes disorder, leading to the highly elongated, uniaxial conformation of mesogens. The *trans/gauche* ratio within the antiferroelectric SmC_A^* remains nearly constant in the whole temperature range, while within the SmI_A^* phase the progressive significant increase of the *trans* population may be observed. The latter effect seems to be the main source of the phase metastability, where the kinetics of the *trans* chain ordering may govern the observed phenomenon. The significant decrease of the 2978 cm^{-1} band intensity, as observed in Figure 6b, may also suggest that the conformational disorder may be somehow driven by the CH_3 dynamics.

The alkyl chain disorder also results in the visible smearing and overlapping of the bands assigned to the terminal part deformations. The scissoring modes are assigned to the bands around 1460 cm^{-1} .³² As one may see in Figure 5, the quoted modes result in a broad overlapped band which is completely “melted”, above the SmI_A^* phase. The rise of *gauche* disorder is reflected in the strongly overlapping region around 1250 cm^{-1} , assigned to $\tau\text{C}-\text{C}$, $\omega\text{C}-\text{C}$, and $\rho\text{C}-\text{C}$ vibrations. The $\nu\text{C}-\text{C}$ stretching modes may be observed near 1100 cm^{-1} . The main differences are related with the crystal \rightarrow liquid crystal phase transition, revealing slight variations as may be expected from Figure 6b. However, due to an extremely complex nature of the discussed bands, the further deconvolution would be meaningless. The significant jump of the related intensities upon the transition into the liquid state is related with the loss of

orientational ordering and the spatial averaging of the corresponding transition dipole moment distributions.

Molecular Cores. Several bands assigned to the central core modes were chosen for further consideration. The temperature dependence of the related band positions is collected in Figure 7, while their normalized integral intensities have been analyzed in Figure 8. The blue points correspond to the cooling cycle, while the red ones stand for the following heating. The bands were labeled with the lowercase letters as in Table 2. The results from the heating cycle reproduce the precedent cooling ones with no noticeable differences.

As might be expected from the reported DSC data, the spectral changes accompanying the phase transitions are very subtle. The band shifting probed within the broad temperature range is smaller than 10 cm^{-1} for all the studied bands. The most prominent changes are related to crystallization and orientational melting to the isotropic phase, while the extremely subtle and progressive changes accompany the transitions within the liquid crystal state. The bands near 1700 cm^{-1} , assigned to the $\nu\text{C}=\text{O}$ modes, shift down significantly upon cooling, where the upper frequency band, related with the carbonyl group at the molecular short axis, reveals the strongest temperature dependence. However, one may see that the band remains nearly constant in the whole mesophase range. An additional drop may be observed with the rise of orientational ordering through the transition from the liquid to SmA^* phase. We may expect that increasing correlation of the transverse dipole moments shifts the frequencies down upon cooling with lowering the attracting interactions between these polar groups.

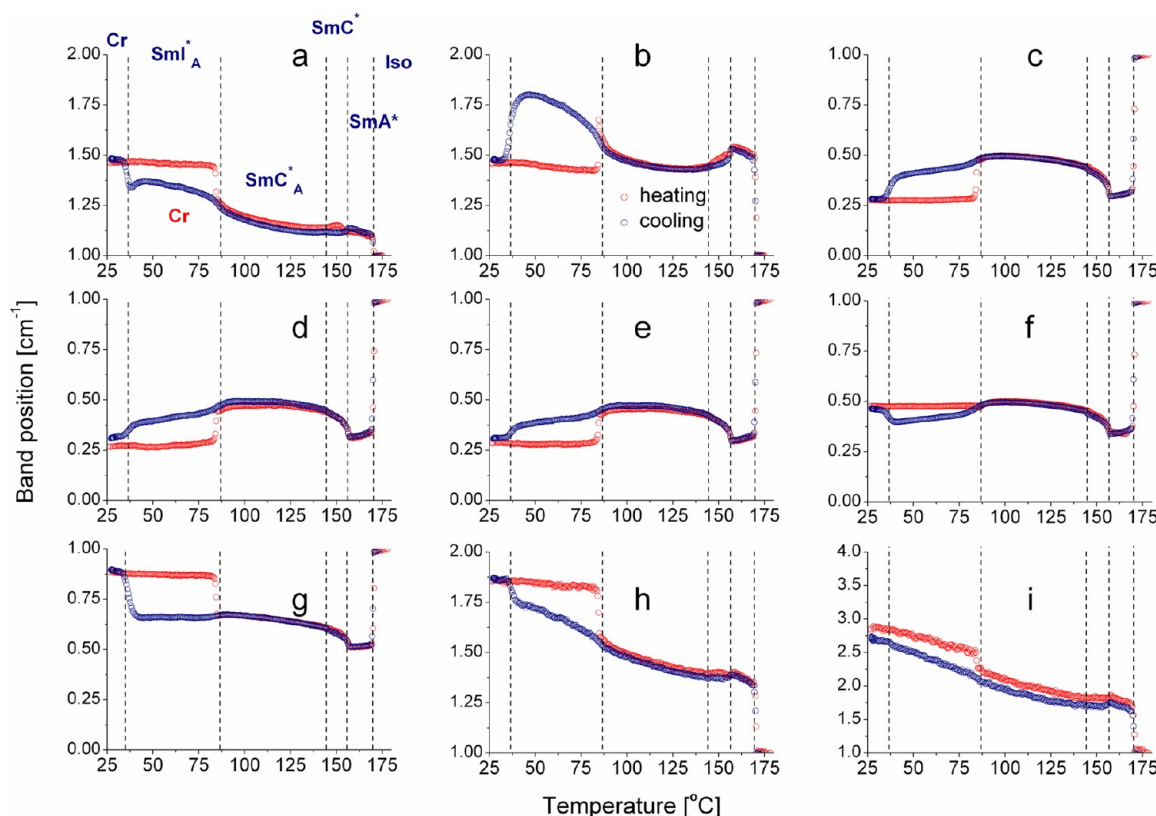


Figure 8. Temperature evolution of the integral intensities for the most prominent bands (corresponding with Figure 2) of the MHPSBO10 sample in homeotropic orientation as observed by temperature-dependent infrared spectroscopy. The intensities normalized with respect to the isotropic phase. Cooling and heating cycles colored in blue and red, respectively. The bands were labeled with the lowercase letters as defined in Table 2.

Table 2. Frequencies of the Most Prominent FT-IR Bands of MHPSBO10 Taken under Study along with Their Approximate Assignment, Polarization, and the α and β Euler Angles Associated with Particular Normal Modes as Observed by Polarized FT-IR and Predicted by DFT Computations^a

band	freq. [cm ⁻¹]	approximate assignment	polar	β FT-IR	φ DFT	β DFT			
				SmA*	B3LYP ^b	B3LYP ^b	PBE ^c	ONIOM ^d	PBC ^e
a	1715	ν C=O (chiral)	\perp	59.8	57.8	59.4	60.6	65.0	81.1
b	1680	ν C=O	\perp	68.9	128.0	69.3	70.0	66.7	73.7
c	1600	ν C=C biPh (ss)	\parallel	172.3	104.9	177.9	175.5	172.1	176.9
d	1527	ν C=C biPh (ass) + ν Ph-Ph	\parallel	167.8	63.6	173.3	171.8	174.5	178.6
e	1500	ν C=C biPh (ass) + ρ C-H (biPh)	\parallel	163.5	48.6	173.2	166.4	172.3	178.6
f	1189	ρ C-H Ph	\parallel	176.4	133.0	170.6	165.7	171.2	176.1
	1180	ρ C-H (biPh)			83.7	173.1	172.5	175.2	177.3
g	900	β CCC biPh + ν C-S	\parallel	156.2	55.7	160.4	161.6	165.6	135.6
h	760	γ Ph-H	\perp	67.3	36.4	65.5	73.2	64.7	65.6
i	690	γ Ph _{trig}	\perp	75.2	34.5	79.8	76.8	68.9	79.1

^aTable Legend: biPh – stands for the biphenyl part; Ph – stands for the phenyl ring linked with the short axis. ^bB3LYP/6-31+G(d). ^cPBE//6-31+G(d). ^dONIOM – PBE/6-31+G(d):3:21+G(d). ^ePBC – CASTEP/ Γ point PBE/NC/1050 eV. For further computational details, see ref 32.

The reverse tendency may be noticed for other perpendicular bands, namely, ~ 760 and 690 cm⁻¹, assigned to the out-of-plane modes of the phenyl ring adjacent to the chiral part. These modes, especially the former one—for which the shift is more noticeable—are related to the phenyl C–H deformations. While the correlation of the transverse dipole moments increases upon cooling, the effective field attracting the C–H bonds lowers, which may result in shifting up of the related wavenumbers. However, in parallel, the thermal rise of the C–H vibration amplitudes may also contribute to this effect. The band which was previously found at 760 cm⁻¹ finally shifts down upon crystallization which comes from the crystal

packing effects. The remaining bands undergo a similar tendency, shifting up with cooling. Most of them are linked with the biphenyl vibrations, hence the increase of the force constants should be expected according to the progressive increase of stacking interactions.

The recorded spectra revealed prominent changes of the integral intensities as presented in Figure 8. Since the long axis component of the related transition dipole moment is not measured when parallel to the incident beam direction, the recorded spectra naturally reveal their strong dependence on the molecular tilt axis. One may clearly observe a sharp drop of the integral intensity for all the parallel bands upon Iso \rightarrow

SmA* transition and the reverse behavior of the perpendicular bands. The c–e bands revealed the same tendency in the whole temperature range, indicating the strong and similar parallelism of the transition dipole moments with respect to the molecular long axis. All these bands may be further used as a probe of the long axis ordering. The bands at ~ 1180 and ~ 900 cm^{-1} reveal the different tendency at lower temperatures. The former one reveals opposite tendency upon crystallization, while in the latter case the band intensity remains constant in the SmI_A* phase, growing significantly at the crystallization. However, in the latter case the transition dipole moment is strongly deviated from the molecular long axis, depending also on the intermolecular interactions, as presented in Table 2.

According to Table 2, there are four bands linked with the transverse dipoles. The bands at ~ 1715 (a) and 760 cm^{-1} (h) are directly related to the chiral part, and their intensities may be used as a further probe of the short axes ordering.

The evolution of the $\nu\text{C}=\text{O}$ band (b) is quite different and interesting. As one may deduce from Figure 3a the longitudinal contribution of the transition dipole moment is negligible here. Table 2 also clearly shows that the β angle is highly perpendicular to the molecular long axis. It is interesting that the temperature dependence of the relative integral intensity within the mesophases is the same and nearly quantitatively exact as the apparent S order parameter reported earlier for some compounds, like MHPOBC or TFMHPNCBC, which reveal a giant electroclinic effect observed below the SmC_A* phase.⁴⁰ It was concluded that in such compounds the results can only be interpreted if the molecular long axes in SmI_A* are not tilted from the layer normal. It is not the case observed in our studies since the molecules are visibly tilted in the hexatic phase, but assuming the strong transversity of the related transition dipole moment geometry, we may deduce that it is nearly perpendicular to the layer normal contributing to the electroclinic effect. The discrepancy between the molecular tilt angles in the hexatic phase determined with infrared and electro-optical studies, which is discussed below, may be partially related to this phenomenon.

Order Parameters. Since the parallel component of the transition dipole moment is not measured in the homeotropic configuration, the absorbance may be expressed as a sum of the A_X and A_Y components. By solving the set of eqs 1 for parallel and perpendicular bands, we can obtain the uniaxial and biaxial order parameters, namely, S and D . For the transition moment strongly parallel to the long molecular axis, the formula can be simplified (because $\beta \approx 180^\circ$) to the term

$$S = 1 - A \quad (9)$$

where A is the absorbance normalized to the isotropic phase.

The order parameter observed in ferroelectric phases is in fact the apparent one⁴¹ since its measured value deviates from the real order parameter by the factor of $P_2(\cos \theta)$.

The real order parameter may be obtained by fitting the power law term in the SmA* phase and extrapolating it down to lower temperatures

$$S' = B(T_c - T)^c \quad (10)$$

where B and c are the constants and T_c stands for the temperature of the transition to the uniaxial phase.

Figure 9 delivers the temperature dependence of the apparent order parameter along with the extrapolation of the real order parameter to lower temperatures. The observed dependence is similar to the previously reported results in the

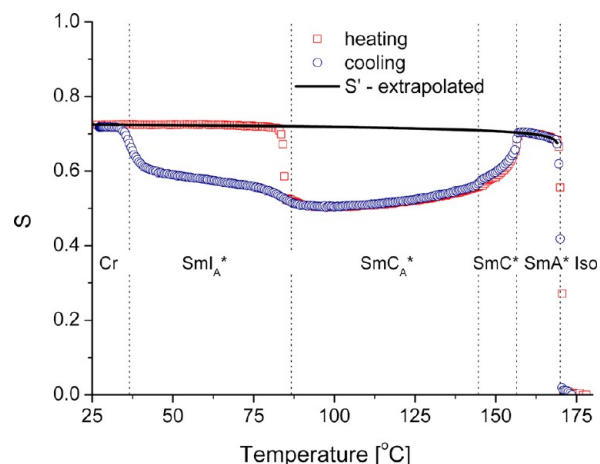


Figure 9. Temperature evolution of the apparent order parameter S recorded for the homeotropic sample of MHPBSO10.

example by Korlacki et al.²³ The strong jump of the parameter from 0 to 0.68 upon the transition from the isotropic to SmA* phase may be observed. The order parameter finally reaches 0.72 in the paraelectric phase, due to the decrease of the thermal fluctuations. The value of the order parameter in the SmA* phase is a measure of the sample ordering, confirming an excellent homeotropic alignment. In practice, such a parameter will never reach 1.0 since, as we will show further on, the molecules are in fact also tilted but equally distributed over the cone. At the transition to the SmC* phase the parameter decreases along with progressive tilting of molecules and increasing sharpness of the dipole distribution. A small discontinuity may be observed upon transition to the SmC_A* phase. The tendency has been preserved in the whole temperature range, saturating at ~ 110 $^\circ\text{C}$. Upon the transition to the hexatic phase, the back increase of the apparent order parameter may be observed along with the change of molecular tilting. The truth orientational order parameter, extrapolated from the SmA* phase using eq 8, saturates near ~ 110 $^\circ\text{C}$, finally reaching the value of 0.72, staying in perfect agreement with the order parameter extrapolated from the SmA* phase.

As presented in Figure 10a, along with the electro-optical results, the analysis of the apparent order parameter allows us to obtain the molecular tilt angle θ , by transforming the equation directly defining the order parameter

$$S = \frac{1}{2} \langle 3 \cos^2 \theta - 1 \rangle \quad (11)$$

into the following form

$$\langle \sin^2 \theta \rangle = \frac{2}{3} (1 - S) \quad (12)$$

The analysis of the tilt angle obtained using both methods reveals a drastic discrepancy in the SmA* phase. The electro-optic results show that θ is close to 0° in the SmA* phase, reaching 10° due to the occurrence of the electroclinic effect in the vicinity of the transition into the ferroelectric phase. However, the FT-IR measurements revealed that the molecules seem to be significantly tilted for $\sim 26^\circ$ with respect to the layers normal. The discrepancy comes from the fact that, although the molecules are tilted, the uniaxial symmetry of the phase causes the optical axis to be in the direction of the layer normal, hence the tilt cannot be observed in the electro-optical studies. To get more information about the nature of the SmA*

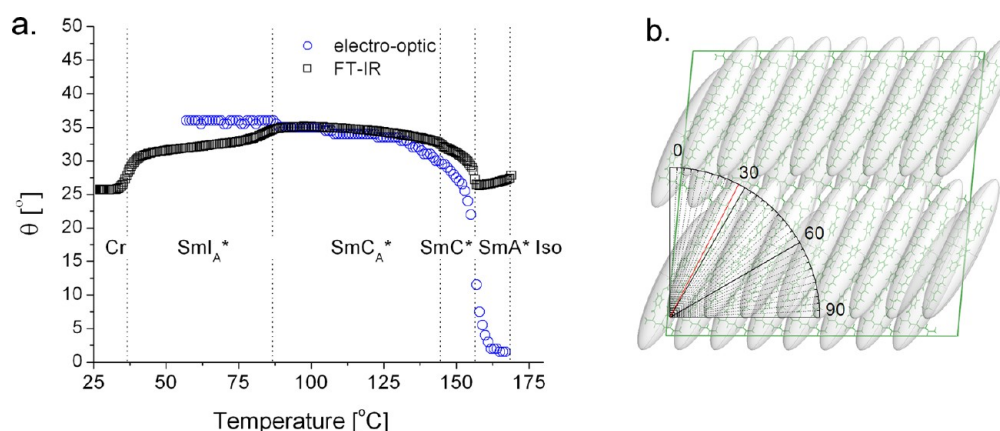


Figure 10. Temperature dependence of the molecular tilt angle θ as seen in MHPSBO10 by FT-IR spectroscopy and electro-optic measurements (a). The X-ray derived crystal phase structure of MHPSBO10 along with the measured tilt angle.

phase, the birefringence measurements have been performed and presented in Figure 11.

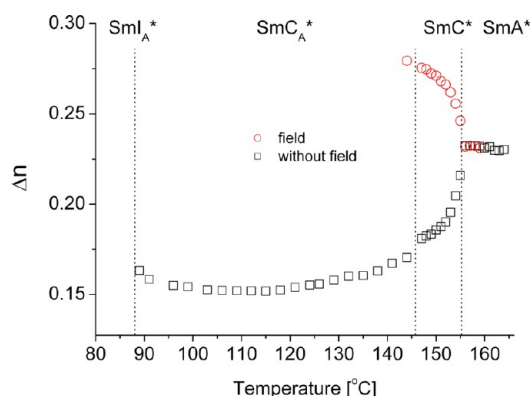


Figure 11. Temperature dependence of birefringence recorded for the MHPSBO10 sample.

By analyzing the set of the performed experiments, we may conclude that the character of the SmA^* phase is not of de Vries type. The significant S order value contradicts with such an assumption.⁴² Moreover, the drop of the parameter at the transition to the ferroelectric was observed.⁴³ Finally, there is no electric field induced increase of the birefringence value within the SmA^* phase.^{44,45} The dielectric studies of the soft mode, as presented in ref 34, also support our conclusion since the fluctuation of this motion is not as strong as in de Vries compounds.⁴⁵

In the ferro-/antiferroelectric phases, the angle is observed at comparable values when using both methods. However, at higher temperatures its value observed with the optical method is noticeably lower than for FT-IR. Although the electric field may additionally influence the value of the observed tilt, the diffused azimuthal distribution of the molecular orientation projects the angle at lower values. Finally, the observed difference vanishes at lower temperatures, near the transition to the hexatic phase, where the antiferroelectric state is fully attained and the spatial distribution is the sharpest. However, in the electro-optically measurable range, down to $\sim 55^\circ\text{C}$, the tilt angle seems to be saturated at $\sim 35^\circ$, which contradicts the decreasing tendency observed with FT-IR. Such an effect is most probably related to the occurrence of the strong electroclinic effect. The previously reported spontaneous

polarization measurements indicate the value to reach 230 nC/cm^2 in this range, even accompanied by a small jump at the transition to the hexatic phase. It seems that the electro-optically measured angle is strongly induced by the coupling of spontaneous polarization and the strong electric field applied. The high values of the spontaneous polarization are also expected due to the strong coupling of the perpendicular dipoles as suggested in Figure 8. Hence, we may assume that the molecular tilt in the SmI_A^* phase decreases with temperature, finally coming back to the value of $\sim 25^\circ$ in the crystal phase. Figure 10b presents the crystal structure calculated with the previously described PBC DFT approach within the unit cell parameters determined with powder X-ray diffraction. The molecular tilt measured for such a structure equals $\sim 27^\circ$, staying in excellent agreement with the FT-IR results.

By solving the set of eqs 1 with respect to a perpendicular band related with the molecular short axis, we can explore the order parameter D

$$D = \frac{2\left(A - 1 - S\left(\frac{3}{2}\sin^2\beta - 1\right)\right)}{\sin^2\beta \cos 2\varphi} \quad (13)$$

By analysis of eq 13, we can find that the D order parameter can be directly probed only if $\sin^2\beta = 2/3$, hence only if the probed transition dipole moment deviates from the molecular long axis at the “magic angle”.

The parameter is defined as a difference in probabilities of finding the molecular axes x and y along the laboratory axis Z . Its value describes the molecular short axes degree of freedom and hence the ordering of the transversal components of the dipole moment. On the whole, the order parameter D may adopt positive, zero, as well as negative values. It is more convenient to analyze the order parameter by rotating the molecular frame, making the φ angle parallel to the x or y axes (multiplying D order expression by the $\cos 2\varphi$ factor, where φ denotes the deviation of the transition dipole moment from the molecular short axis). In such a case, a positive D value indicates that the absorption band under consideration is due to a transition moment which projects predominantly on the preferred pivoting axis. The opposite case is indicated by a negative value of D . Such a parameter equals zero if the related transition moment projects equally on both axes or if none of the pivoting axes is preferred as in the case of free rotation or for the cylindrically symmetric molecules.⁴⁶

To probe the transverse order parameter, the reported S has been taken along with the band assigned to the $\nu\text{C}=\text{O}$ vibration at the chiral part. The corresponding transition dipole moment deviates from the long axis for $\beta \approx 60^\circ$, being oriented exactly parallel to the adjacent phenyl ring plane. The integral intensity of the 1715 cm^{-1} band is much larger than the intensity of the 760 or 690 cm^{-1} ones. The weaker the transition dipole strength, the bigger the changes of the relative integral intensity observed, and the band is more fragile for the pivoting amplitude. A values of 1715 cm^{-1} is also a better candidate since β is closer to the “magic angle” value, and hence the obtained parameter is less dependent on the S parameter. The calculated D has been followed with temperature and presented in Figure 12.

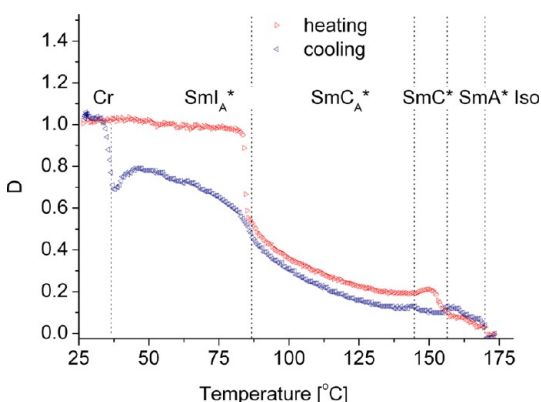


Figure 12. Temperature evolution of the D order parameter determined using the $\sim 1715\text{ cm}^{-1}$ band for the homeotropic sample of MHPBSO10.

The determined D values in our case vary from 0 to 1. By cooling the sample and transforming the system into the SmA^* phase we observe a very slight rise of the order parameter up to ~ 0.1 since none of the pivoting axes is preferred due to the expected free molecular rotation. As concluded before, the highly elongated conformation in the SmA^* and SmC^* phases may be expected. A small pretransitional effect in the vicinity of *para*-ferroelectric transition may be found, which may be linked with sharpening of molecular distribution over the cone. Then, probably the emergence of the helical structure slightly decreases the observed D values which remain constant within the SmC^* phase. Within the antiferroelectric phase we observe significant exponential rise of the order parameter from ~ 0.1 up to ~ 0.5 . Such an effect supports our previous studies revealing high, progressively growing values of spontaneous polarization and rotational viscosity along with a significant decrease of the dielectric increment. Such behavior was progressive also in the range where the molecular tilt angle was nearly constant. This effect may be explained based on the theory developed by Gleeson et al.,⁴⁷ which claims that such behavior may be directly linked to a coupling between the spontaneous polarization and the biaxial order parameter. Upon the transition to the crystal-like hexatic phase, the parameter inflects, and such behavior was also reflected in the quoted macroscopic parameter studies. The above-reported S order parameter along with the tilt angle suggests that the sample has crystallized in a highly ordered way. Hence, it is convenient to further analyze D evolution using the crystal structure as a point of reference. We can expect that D should reach the highest values since the head-to-tail distributed, synclinal tilted

molecules are strongly correlated, being uniformly oriented along the direction of their short axes, and the molecular reorientations are frozen here. In the SmI_A^* which may be described as an anticlinic, D progressively grows upon cooling in the whole phase range, until the pretransitional effect occurs. Then, the short axes correlation suddenly drops close to the level of the $\text{SmC}_A^* \rightarrow \text{SmI}_A^*$, and the sample crystallizes. We can assume that in the SmI_A^* phase the molecules are significantly tilted for $\sim 32^\circ$ toward the apex of the hexagon. By analyzing the temperature dependence of the central core $\nu\text{C}=\text{O}$ absorbance (as illustrated in Figure 8b), one may see that the correlation of the related central core dipoles reaches maximum in this phase. Hence, we may assume that the central cores, as well as the related $\text{C}=\text{O}$ groups, are in maximal contact with each other, being possibly oriented in one direction. Our previous studies³⁴ revealed extremely high values of the rotational viscosity, which seems to support this assumption. As the population of *trans* conformers is growing, the molecules as a whole are elongating; the $\text{C}=\text{O}$ groups are separating; and the molecular tilt decreases. It is accompanied by increasing correlation of the short axes as indicated by D evolution. Finally, we observe the rapid loss of the short axes correlation which is accompanied by the significant drop of the central core $\nu\text{C}=\text{O}$ absorbance. This pretransitional effect may be linked to the final reorientation of the molecular cores. The central $\text{C}=\text{O}$ groups are separating from each other, and the $\pi-\pi$ stackings stabilize the biphenyl coplanarity. The lowering of the D parameter may be related to the rebuilding of the system, leading to the synclinal structure of the crystal phase. This phenomenon may be directly driven by conformational jumps of the $\text{C}=\text{O}$ groups at the chiral part since both conformations are equally probable. Such an assumption seems to be confirmed by the temperature dependence of the out-of-plane phenyl deformation modes at 760 and 690 cm^{-1} (see Figure 8 h and i), where no such effect can be observed.

CONCLUSIONS

The temperature-dependent infrared studies of MHPBSO10 have been presented revealing the influence of phase transition on the vibrational spectrum of the studied compound. The experimental data have been supported by theoretical computations giving further insight into the nature of the absorption bands by detailed analysis of the transition dipole moments. The recorded spectra revealed a strong dependence on the molecular tilt angle, giving an opportunity to probe this parameter in detail and delivering a consistent picture of the structural phase properties. The main order parameters have been followed with temperature, and the strong hindrance of molecular reorientations has been observed, clarifying significantly large values of selected macroscopic properties observed in our previous studies.

AUTHOR INFORMATION

Corresponding Author

*E-mail: druzbick@chemia.uj.edu.pl.

Notes

The authors declare no competing financial interest.

ACKNOWLEDGMENTS

The authors would like to express their appreciation for the kind help of Ms. Ewa Hylewska and Prof. Roman Wrzaliak in the experimental work. This research was supported by PL-Grid

Infrastructure (Grant ID: druzbicki, Zeus Supercomputer). The computations were also done at the Academic Computer Centre CYFRONET AGH, Cracow, Poland (Grants ID: MNiSW/SGI3700/UJ/007/2009 - Baribal Supercomputer; MNiSW/IBM_BC_HS21/UJ/032/2009 - Mars Supercomputer). Calculations with Materials Studio 5.5 were performed within Accelrys Polish national license.

REFERENCES

- (1) Neff, V. D.; Gulrich, L. W.; Brown, G. H. In *Liquid Crystals*; Brown, G. H., Dienes, G. D., Labes, M. M., Eds.; Gordon Brown: New York, 1967.
- (2) Maier, W.; Saupe, A. Z. *Naturforsch.* **1961**, *16a*, 816–816.
- (3) Bulkin, B. J. *Appl. Spectrosc.* **1976**, *30*, 261–269.
- (4) Kirov, N.; Simova, P. *Vibrational spectroscopy of liquid crystals*; Pub. House of the Bulgarian Academy of Sciences: Sofia, Bulgaria, 1984.
- (5) Simova, P.; Ratajczak, H.; Kirov, N.; Fontana, M. P. *Atlas of vibrational spectra of liquid crystals*; World Scientific: New Jersey, 1988.
- (6) Fontana, M. P.; Rosi, B.; Kirov, N.; Dozov, I. *Phys. Rev. A* **1986**, *33*, 4132–4142.
- (7) Fontana, M. P. The Molecular Dynamics of Liquid Crystals Proceedings of the NATO Advanced Study Institute on The Molecular Dynamics of Liquid Crystals II Ciocco. Barga, Italy September 11–23, 1989. *NATO Sci. Ser.* **1994**, *431*, 403–428.
- (8) Janik, J. A.; Godlewska, M.; Grochulski, T.; Kocot, A.; Sciesinska, E.; Sciesinski, J.; Witko, W. *Mol. Cryst. Liq. Cryst.* **1983**, *98*, 67–81.
- (9) Godlewska, M.; Janik, J. A.; Kocot, A.; Nguyen, X. P.; Sciesinski, J.; Witko, W. *Liq. Cryst.* **1986**, *1*, 529–537.
- (10) Kocot, A.; Kruk, G.; Wrzalik, R.; Vij, J. K. *Liq. Cryst.* **1992**, *12*, 1005–1012.
- (11) Hild, E.; Kocot, A.; Vij, J. K.; Zentel, R. *Liq. Cryst.* **1994**, *16*, 783–803.
- (12) Kruk, G.; Kocot, A.; Wrzalik, R.; Vij, J. K. *Liq. Cryst.* **1993**, *14*, 807–819.
- (13) Perova, T. S.; Kocot, A.; Vij, J. K. *SPIE* **1996**, *2731*, 107–115.
- (14) Kocot, A.; Wrzalik, R.; Vij, J. K. *Liq. Cryst.* **1996**, *21*, 147–151.
- (15) Sigarev, A. A.; Vij, J. K.; Panarin, Yu. P.; Rudquist, P.; Lagerwall, S. T.; Heppke, G. *Liq. Cryst.* **2003**, *30*, 149–156.
- (16) Sigarev, A. A.; Vij, J. K.; Panarin, Yu. P.; Goodby, J. W. *Ferroelectrics* **2000**, *245*, 27–34.
- (17) Sigarev, A. A.; Vij, J. K.; Fukuda, A.; Jin, B.; Takanishi, Y. *Ferroelectrics* **2004**, *311*, 97–109.
- (18) Sigarev, A. A.; Vij, J. K.; Hall, A. W.; Cowling, S.; Goodby, J. W. *Ferroelectrics* **2006**, *343*, 167–175.
- (19) Kim, K. H.; Takanishi, Y.; Ishikawa, K.; Takezoe, H.; Fukuda, A. *Liq. Cryst.* **1994**, *16*, 185–202.
- (20) Kim, K. H.; Ishikawa, K.; Takezoe, H.; Fukuda, A. *Phys. Rev. E* **1995**, *51*, 2166–2175.
- (21) Kim, K. H.; Miyachi, K.; Ishikawa, K.; Takezoe, H.; Fukuda, A. *Jpn. J. Appl. Phys.* **1994**, *33*, 5850–5859.
- (22) Ossowska-Chrusciel, M. D.; Korlacki, R.; Kocot, A.; Wrzalik, R.; Chrusciel, J.; Zalewski, S. *Phys. Rev. E* **2004**, *70*, 041705(1)–041705(10).
- (23) Korlacki, R.; Fukuda, A.; Vij, J. K.; Kocot, A.; Görtz, V.; Hird, M.; Goodby, J. W. *Phys. Rev. E* **2005**, *72*, 041704(1)–041704(9).
- (24) Hayashi, N.; Kocot, A.; Linehan, M. J.; Fukuda, A.; Vij, J. K.; Heppke, G.; Naciri, J.; Kawada, S.; Kondoh, S. *Phys. Rev. E* **2006**, *74*, 051706(1)–051706(11).
- (25) Kocot, A.; Vij, J. K. *Liq. Cryst.* **2011**, *38*, 663–668.
- (26) Merkel, K.; Nagaraj, M.; Kocot, A.; Kohlmeier, A.; Mehl, G. H.; Vij, J. K. *J. Chem. Phys.* **2012**, *136*, 094513–094522.
- (27) Merkel, K.; Kocot, A.; Vij, J. K.; Mehl, G. H.; Meyer, T. *J. Chem. Phys.* **2004**, *121*, S012–S021.
- (28) Korlacki, R.; Merkel, K.; Vij, J. K.; Wrzalik, R.; Kocot, A.; Ossowska-Chrusciel, M. D.; Chrusciel, J.; Zalewski, S. *Liq. Cryst.* **2006**, *33*, 219–225.
- (29) Wrzalik, R.; Merkel, K.; Kocot, A.; Cieplak, B. *J. Chem. Phys.* **2002**, *117*, 4889–4896.
- (30) Korlacki, R.; Steiner, M.; Meixner, A. J.; Vij, J. K.; Hird, M.; Goodby, J. W. *J. Chem. Phys.* **2007**, *126*, 224904–224908.
- (31) Druzbicki, K.; Mikuli, E.; Ossowska-Chrusciel, M. D. *Vib. Spectrosc.* **2010**, *52*, 54–62.
- (32) Druzbicki, K.; Mikuli, E.; Kocot, A.; Ossowska-Chrusciel, M. D.; Chrusciel, J.; Zalewski, S. *J. Phys. Chem. A* **2012**, *116*, 7809–7821.
- (33) Ossowska-Chrusciel, M. D.; Chrusciel, J. *Thermochim. Acta* **2010**, *502*, 51–59.
- (34) Druzbicki, K.; Mikuli, E.; Zalewski, S.; Ossowska-Chrusciel, M. D.; Chrusciel, J.; Wróbel, S.; Czerwiec, J. *Mater. Chem. Phys.* **2012**, submitted.
- (35) Clark, S. J.; Segall, M. D.; Pickard, C. J.; Hasnip, P. J.; Probert, M. J.; Refson, K.; Payne, M. C. *Z. Kristallogr.* **2005**, *220*, 567–570.
- (36) Kocot, A.; Wrzalik, R.; Orgasinska, B.; Perova, T.; Vij, J. K.; Nguyen, H. T. *Phys. Rev. E* **1999**, *59*, 551–555.
- (37) Larsson, K.; Rand, R. P. *Biochim. Biophys. Acta* **1973**, *326*, 245–255.
- (38) Harder, P.; Grunze, M.; Dahint, R.; Whitesides, G. M.; Laibinis, P. E. *J. Phys. Chem. B* **1998**, *102*, 426–436.
- (39) Atkinson, J. R.; Biddlestone, F.; Hay, J. N. *Polymer* **2000**, *41*, 6965–6968.
- (40) Korlacki, R.; Fukuda, A.; Vij, J. K. *Europhys. Lett.* **2007**, *77*, 36004–36009.
- (41) Hayashi, N.; Kato, T. *Phys. Rev. E* **2001**, *63*, 21706(1)–21706(10).
- (42) Korlacki, R.; Panov, V. P.; Fukuda, A.; Vij, J. K.; Spillmann, Ch. M.; Naciri, J. *Phys. Rev. E* **2010**, *82*, 031702(1)–031702(7).
- (43) Gorkunov, M. V.; Giesselmann; Lagerwall, J. P. F.; Sluckin, T. J.; Osipov, M. A. *Phys. Rev. E* **2007**, *75*, 060701R(1)–060701R(4).
- (44) Manna, U.; Song, J. K.; Panarin, Y. P.; Fukuda, A.; Vij, J. K. *Phys. Rev. E* **2008**, *77*, 041707(1)–041707(12).
- (45) Lagerwall, S. T.; Rudquist, P.; Giesselmann, F. *Mol. Cryst. Liq. Cryst.* **2009**, *510*, 148–157.
- (46) Korte, E. H. *Mol. Cryst. Liq. Cryst.* **1983**, *100*, 127–135.
- (47) Gleeson, H. F.; Wang, Y.; Watson, S.; Sahagun-Sanchez, D.; Goodby, J. W.; Hird, M.; Petrenko, A.; Osipov, M. A. *J. Mater. Chem.* **2004**, *14*, 1480–1485.